CLIMATOLOGY

Anthropogenic warming has ushered in an era of temperature-dominated droughts in the western United States

Yizhou Zhuang[1], Rong Fu[1]*, Joel Lisonbee[2,3], Amanda M. Sheffield[2,3], Britt A. Parker[2], Genoveva Deheza[2]

Historically, meteorological drought in the western United States (WUS) has been driven primarily by precipitation deficits. However, our observational analysis shows that, since around 2000, rising surface temperature and the resulting high evaporative demand have contributed more to drought severity (62%) and coverage (66%) over the WUS than precipitation deficit. This increase in evaporative demand during droughts, mostly attributable to anthropogenic warming according to analyses of both observations and climate model simulations, is the main cause of the increased drought severity and coverage. The unprecedented 2020–2022 WUS drought exemplifies this shift in drought drivers, with high evaporative demand accounting for 61% of its severity, compared to 39% from precipitation deficit. Climate model simulations corroborate this shift and project that, under the fossil-fueled development scenario (SSP5-8.5), droughts like the 2020–2022 event will transition from a one-in-more-than-a-thousand-year event in the pre-2022 period to a 1-in-60-year event by the mid-21st century and to a 1-in-6-year event by the late-21st century.

INTRODUCTION

The western United States (WUS) has been experiencing a prolonged dry period in the 21st century. The first two decades have been characterized by extended periods of extremely low precipitation, record-setting heat waves, and a substantial decline in the Colorado River flow, which have led to imposed water restrictions and reduced hydropower production (*1*–*4*). This contemporary dry period is comparable to the worst "megadrought" in the paleoclimatic records (*5*–*7*) and may represent a warming-induced shift toward a more arid climate for the region (*8*–*10*).

Recent droughts in the WUS have been costly and far-reaching. The 2020–2022 drought experienced frequent power shortages from hydropower production, intense and widespread wildfires, low reservoir inflows, reduced agricultural productivity, and ecosystem degradation (*3*). Other studies on recent drought impacts show surges in respiratory and cardiovascular diseases, mental health disorders, and other public health issues associated with drought (*11*). These impacts are caused not only by precipitation deficit but also by high temperature and the resulting evaporative demand.

Meteorological droughts usually result from the cumulative imbalance between precipitation and evaporative demand. Historically, precipitation deficit has been the dominant factor in WUS droughts, whereas evaporative demand, largely controlled by surface temperature (Materials and Methods and fig. S1), has been a minor contributor to drought severity (*12*, *13*). However, as surface temperatures continue to rise in recent decades, droughts have become not only more pervasive but also more impactful over the WUS. The increasing concurrence and coupling between precipitation deficit and heat waves amplify water and energy demands; intensify heat and water stresses for humans, animals, and plants; and worsen air and water pollution (*14*). These changes are broadening the scope of drought dynamics and impacts, challenging our traditional precipitation deficit–centered definition, understanding, monitoring, and management strategy of droughts. As the temperature-driven increase in evaporative demand becomes a main drought driver (*3*), droughts in the WUS will be more intense, last longer, and become more frequent and widespread despite uncertainties in future precipitation changes. Has a tipping point been reached? Has the main drought driver shifted from precipitation deficit to high evaporative demand? If so, when did this change occur? To what extent can long-term changes in these two drivers be attributable to climate change versus natural climate variability, and how have these changes contributed to increasing drought severity and coverage over the WUS? Answering these questions will provide insight into needed adaptation measures for future droughts.

The role of temperature or evaporative demand in drought has been explored in previous studies. Research has indicated that evaporative demand has become an increasingly impactful contributor to the prolonged dryness and droughts over the WUS (*3*, *5*, *6*, *15*–*18*). They found, for example, that temperature has increasingly contributed to droughts in the 21st century compared to previous periods (*18*). Precipitation deficit and high temperature often co-occur during major drought events in current and paleoclimates over the WUS (*19*–*21*). However, these studies did not quantify whether precipitation deficit or temperature-induced high evaporative demand is the leading cause. Although the increase in air temperature has led to higher evaporative demand and increased drought severity, existing research studies (*22*–*24*) have indicated that precipitation still remains the primary driver of drought in the past and current climate over the WUS, among other regions. However, the rapid increases in vapor pressure deficit (VPD) over the most recent decade, especially during the 2020–2022 drought (*3*), highlight the potential for evaporative demand to rival or even surpass precipitation deficit as a primary drought driver, and the urgent need to investigate such a possibility.

[1]Department of Atmospheric and Oceanic Sciences, University of California, Los Angeles, Los Angeles, CA 90095, USA. [2]NOAA National Integrated Drought Information System, Boulder, CO 80305, USA. [3]Cooperative Institute for Research in the Environmental Sciences, University of Colorado Boulder, Boulder, CO 80309, USA.
*Corresponding author. Email: rfu@atmos.ucla.edu

Previous observational studies have demonstrated the influences of precipitation and evaporative demand on droughts (*16*, *22*, *23*, *25*, *26*) without explicitly evaluating the temporal evolution of these changes or disentangling the influences of natural variability versus anthropogenic forcing. Because both natural variability and anthropogenic forcing can modulate the relative contributions of precipitation versus evaporative demand, distinguishing their individual roles in droughts is crucial for determining whether the observed changes are natural and cyclical or long-term driven by climate change. Climate model simulations have been used to investigate the influences of climate change (*27*, *28*). However, many climate models used in these studies do not accurately represent the observed variations at regional scales, such as over the WUS with complex topography, diverse landscapes, and high natural climate variability. To address this gap, we apply a recently developed observation-based circulation analog approach (*29*) to quantify the influences of natural climate variability and anthropogenic warming on both precipitation and evaporative demand anomalies, complementing the model-based attribution studies. The unique strength of this approach is its ability to more realistically quantify the contribution of natural climate variability to the observed variations in precipitation and evaporative demand than done by climate model simulations. This, in turn, allows a more realistic estimate of climate change's influence on the observed changes in these variables of interest (*29*). We also compare our observation-based results to those based on climate model simulations, confirming the robustness of the shift in drought drivers, and investigate how model-projected increases in evaporative demand will affect drought severity and frequency over the WUS in the foreseeable future.

RESULTS

Determine the changes in drought severity, coverage, and drivers

Warming temperatures enhance the atmosphere's capacity to hold water vapor, leading to increased evaporative demand at the land surface. Evaporative demand is commonly quantified by VPD (*3*) or potential evapotranspiration (PET) (*30*). Although VPD is simpler and widely used, it cannot be directly compared to precipitation deficit due to differences in their units. We have chosen to use PET because it quantifies the maximum moisture flux leaving the surface due to evaporative demand and is directly comparable to precipitation (P). The Climatic Research Unit (CRU) data (*31*) are a popular choice for PET analysis (*22*, *25*); however, this dataset has an unrealistic wetting trend in the southwestern US (*32*) (Supplementary Text and figs. S2 and S3) that contradicts more recent research findings (*33*). Thus, we use the fifth-generation European Centre for Medium-Range Weather Forecasts (ECMWF) atmospheric reanalysis (ERA5) (*34*) for PET-related variables and Climate Prediction Center (CPC) precipitation (*35*) data, for their long-standing records, availability of daily data, and proven reliability (*33*, *36*). For simplicity, we will refer to the P or PET calculated from these observation-constrained reanalyses as "observed" hereafter.

We use P′−PET′ to gauge drought severity, a widely accepted approach in the literature (*22*, *30*, *37*–*39*), where P′ and PET′ are deviations of P and PET from their respective 1948–1999 climatological averages, with the seasonal cycle removed (Materials and Methods). To focus on long-term droughts because they have stronger impacts on hydrology and ecology, we use the 12-month moving cumulative P′−PET′ (assigned to the last month of each sliding 12-month window). For example, the drought severity reported for September 2020 reflects the cumulative P′−PET′ from October 2019 through September 2020. Throughout this study, we refer to this 12-month moving cumulative P′−PET′ as P′−PET′, unless stated otherwise. Drought periods are defined when P′−PET′ falls below its local 30th percentile value (calculation of P′−PET′ percentile are detailed in Materials and Methods) for the climatological period of 1948–1999, a percentile threshold recommended by the US Drought Monitor (USDM) (*40*). The relative importance of precipitation and evaporative demand during drought periods can be evaluated by the ratio of P′/(P′−PET′) and −PET′/(P′−PET′), respectively. The negative sign before the PET′ term indicates that higher PET′ (greater evaporative demand) reduces available moisture and thus worsens drought severity.

P′−PET′ exhibits a strong correlation with soil moisture data from various sources and other drought indices (Supplementary Text, fig. S4, and table S1) used by the USDM (*40*), such as the Palmer Drought Severity Index and Palmer moisture anomaly index (Z-index) (*41*). However, PET′ is higher than the actual evapotranspiration anomaly over the WUS when soil moisture cannot meet the evaporative demand. As such, P′−PET′ has larger magnitudes than actual soil moisture loss, especially in semiarid and arid regions with limited soil water capacity, such as the southwestern US (Supplementary Text and figs. S5 and S6). In this regard, while P′−PET′ could overestimate drought severity when compared to soil moisture anomalies, especially in arid regions, this is not necessarily an overestimation of drought impact in general. Higher PET′ often implies drought impacts beyond those of increased evapotranspiration or decreased soil moisture, such as escalating plant water stress and water demand (*42*), which are not captured by soil moisture alone. However, our study does not aim to determine whether such overestimation actually occurs or whether P′−PET′ accurately captures the broader drought effects on agricultural and ecological systems. Rather, we focus on partitioning the relative contributions of P′ and PET′ to the observed drought conditions, based on the demonstrated overall consistency between P′−PET′ and soil moisture anomalies within our study region.

We demonstrate the influence of P′ and PET′ on drought severity and coverage in 1948–2022 over the WUS in Fig. 1. The time series in Fig. 1A shows the evolution of drought severity P′−PET′ and its two components, P′ and −PET′. Throughout most of the period, the mean P′−PET′ closely follows its P′ component most of the time, especially before the 21st century. The PET′ component generally has a smaller amplitude than P′. However, since around 2000, PET′ has increased in magnitude as a response to regional warming, leading to its greater amplitude than P′ in almost all dry periods. Comparing the periods of 1948–1999 (P1) and 2000–2022 (P2), we observe a significantly ($P < 0.01$) more negative P′−PET′ and −PET′ (drought severity in table S2), indicating an increasing surface moisture loss to the atmosphere, from P1 to P2, for all time in general and for the identified WUS drought period (highlighted in yellow); however, changes in P′ are insignificant ($P > 0.1$). This trend in PET′ has led to the doubling of its contribution to drought severity during drought periods from 31% in P1 to 62% in P2 (table S3).

Figure 1B shows the evolution of drought coverage (defined as the grid points where local P′−PET′ values fall below their 30th percentile threshold values), with a decrease from the 1950s to the late 1980s and a subsequent increase, reflecting dry periods in the 1950s to 1960s and post-2000, and a wet period in-between, which is likely associated with the phase shift in the Pacific Decadal Oscillation, according to previous studies (*43*). Drought coverage in earlier

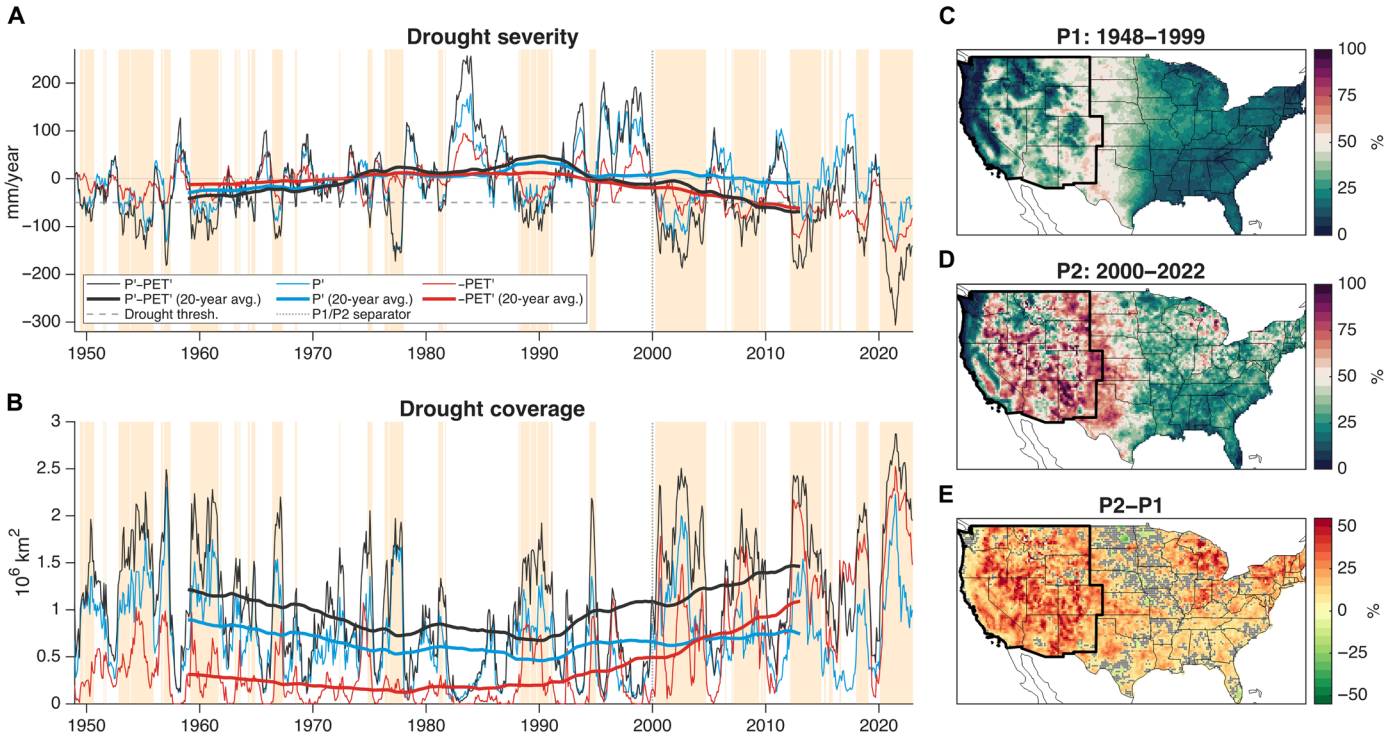

Fig. 1. Contributions of P′ and PET′ to the WUS drought. (**A**) Drought severity time series of 12-month moving cumulative P′−PET′, P′, and −PET′ during 1948–2022 averaged over the WUS (with cosine latitude weighting); the thin lines represent 12-month cumulative values, while the thick lines are their 20-year moving average; the yellow-shaded area represents drought periods identified when average P′−PET′ falls below its 30th percentile value for the 1948–1999 climatological period (marked by the gray dashed horizontal line); the vertical dotted line separates 1948–1999 (P1) and 2000–2022 (P2). We multiply PET′ by −1 for direct comparison with P′. (**B**) Time series of drought coverage and contributions from P′ and −PET′; thin lines represent total areas within the WUS (11 contiguous US states, 3.12×10^6 km^2 in total) that are in drought condition (local P′−PET′ below the 30th percentile value for any grid point; black) and those where PET′ (red line) or P′ (blue line) alone was strong enough to cause drought (Materials and Methods); thick lines are their 20-year moving average. (**C**) Map of averaged PET′ contribution to drought severity, i.e., −PET′/(P′−PET′), during drought periods in P1; the thick black line marks the boundary of the WUS region. (**D**) Same as (C), but for drought periods in P2. (**E**) Change of PET′ contribution from P1 to P2, i.e., the difference between (D) and (C); gray dotted areas indicate insignificant change ($P \geq 0.05$; P values are adjusted using the false discovery rate (FDR) criterion of $\alpha_{FDR} < 0.05$).

drought periods was predominantly influenced by P′. To determine the contribution of P′ to the drought coverage, we first set PET′ to zero and then identify grid points where P′ alone can cause P′−PET′ to reach drought status (Materials and Methods). PET′ contribution is quantified in a similar way by setting P′ to zero. We estimate that P′ accounted for 73% of the drought coverage on average in P1, significantly ($P < 0.01$) larger than the PET′ contribution of 26%; however, in P2, PET′ contribution has increased to 66%, surpassing 55% by P′ (table S3). Note that, in some regions, both P′ and PET′ alone are large enough in magnitude to cause droughts. Because the drought coverage due to P′ and PET′, respectively, is not mutually exclusive, the sum of their fractional coverage can exceed 100%. Further details on the full decomposition of drought coverage can be found in the Supplementary Text and table S4. These results indicate that the rise in PET′ is the primary driver behind the intensification of drought severity and the expansion of drought coverage, shifting the main contributor from P′ in the 20th century (P1) to PET′ in the 21st century (P2). Detailed statistics on changes in drought severity and coverage from P1 to P2 are included in table S2, and contributions of P′ and PET′ are detailed in table S3.

Next, we analyze the spatial variations in PET′ contribution to drought severity across the WUS to identify regions where the impact of evaporative demand on drought severity has significantly ($P < 0.05$) changed from P1 to P2. When the ratio −PET′/(P′−PET′) exceeds 50% during a drought period, it indicates that the evaporative demand contributes more to drought severity than precipitation deficit. We identify the grid points where this ratio is above 50% and calculate the areas they cover. Our result shows that, in P1, PET′ dominated less than one-third of the WUS area (Fig. 1C), whereas, in P2, the dominance of PET expanded to more than half of the WUS, particularly affecting the southwestern US (Fig. 1D). Overall, from P1 to P2, increases in PET′ contributions are observed across most of the WUS (Fig. 1E). By identifying grid points with significant changes [$P < 0.05$, adjusted for false discovery rate (FDR) control (*44*) at 0.05 level; Materials and Methods], we estimate that 93% of the WUS areas exhibit statistically significant changes ($P < 0.05$). This increase is particularly noticeable in Southern California, Nevada, and the Four Corners region. Consequently, PET′ has transitioned from a minor contributor to drought in the 20th century to an equal or even greater contributor than P′ to drought severity across most of the WUS in the 21st century.

Quantify the influences of natural climate variability and human-induced climate change

Drought varies naturally on annual, decadal, and centennial scales. It can be difficult to separate the contributions of natural climate variability to drought from that of anthropogenic climate change. Past droughts were mostly driven by the natural variability of the ocean through its influence on atmospheric circulation and associated feedback mechanisms (*7*). Large ensemble climate model simulations have been commonly used to isolate the impact of anthropogenic climate change (*5*, *6*, *45*). However, these simulations either have random natural climate variability without real-time information or show notable biases in the atmospheric models forced by observed sea surface temperature (*46*). To realistically estimate the influence of natural climate variability on droughts and complement the modeling approaches, we apply an observation-based ensemble constructed flow analog approach (*29*) to estimate P′ and PET′ induced by atmospheric circulation variation (Materials and Methods; "analog anomalies" hereinafter). The residual anomaly, i.e., the difference between observed and analog anomalies, represents variations beyond those that can be explained by circulation changes. They are mainly due to thermodynamic factors, especially anthropogenic forcings and their associated feedback. Because atmospheric circulation anomalies over the WUS are mostly controlled by natural climate variability (*29*, *43*), we assume that the analog P′ and PET′ are due to natural climate variability following (*29*). Note that this assumption neglects the potential anthropogenically forced atmospheric circulation change. Thus, the analog trend likely represents the upper bound of natural variability (*47*, *48*), and the residual trend likely represents the lower bound of anthropogenically forced climate change and its feedbacks.

We apply this analog approach to assess how much natural climate variability and its resulting weather pattern variations have contributed to the observed changes of drought severity P′−PET′ and its two components (Fig. 2). Figure 2A shows that observed P′ largely aligns with analog P′, indicating that natural variability is the dominant factor. While previous studies (*16*) identified an increasing precipitation trend in the region, we did not find a statistically significant change in observed P′ from P1 to P2 (Materials and Methods, fig. S7, A and D; and table S2). There are instances where observed P deficits exceed those of analog in magnitude, particularly when P′ exhibits a greater amplitude, in line with the expected impact of strong thermodynamic feedback associated with strong atmospheric circulation anomalies. For PET′, observed values match well with the analog values in P1 (Fig. 2B), suggesting that natural climate variability also dominated PET′. However, in P2, the gap between observed and analog PET′ has widened considerably, driven by the positive trend in observed PET′. The similar distribution of analog PET′ in P1 and P2 (fig. S7, B and E) suggests no significant changes in the natural variability of PET′ between P1 and P2. As such, the anthropogenic warming (residual) is mainly responsible for the observed changes in PET′ from P1 to P2 for both all-time and drought periods (more detailed statistics in table S5), qualitatively consistent with previous studies on VPD (*5*, *6*, *29*, *45*). Notably, the disparities between observed and analog PET′ or P′−PET′ are more pronounced during drought periods than during non-drought periods (fig. S7) and nearly doubled during all three major droughts over the WUS since 2005

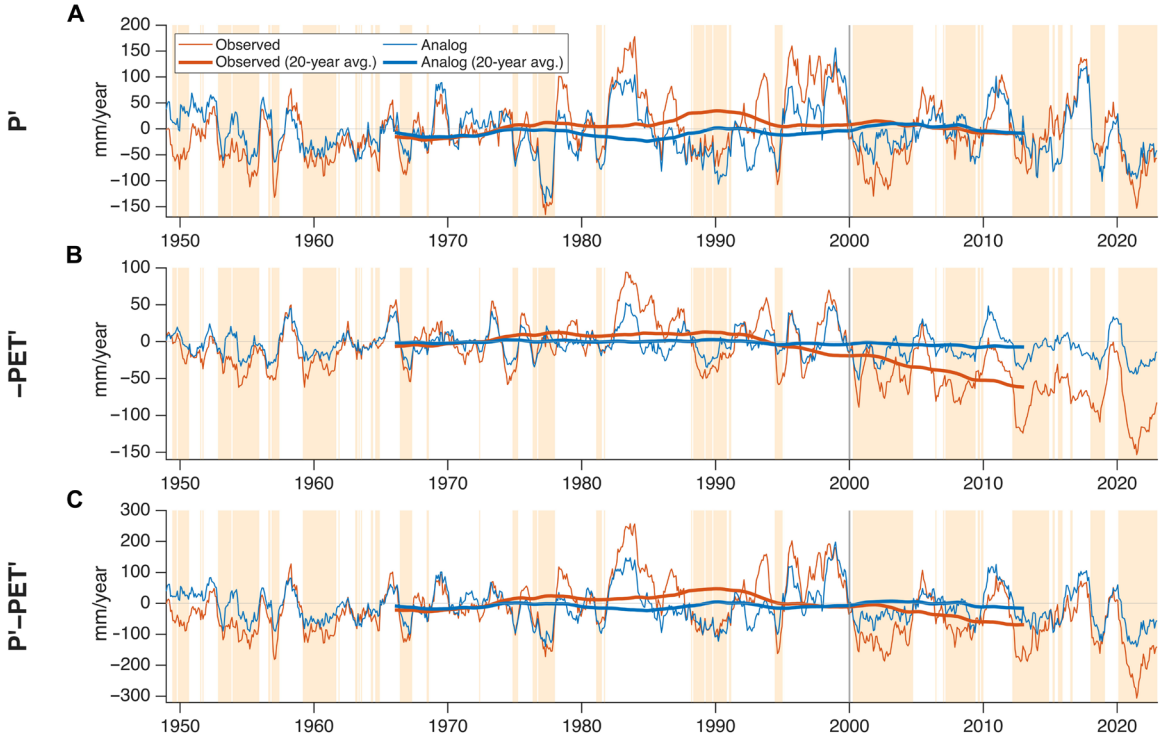

Fig. 2. Circulation contribution (analog) to the observed drought severity and its P′ and PET′ components. Twelve-month moving cumulative time series (thin lines) and 20-year moving averages (thick lines) of (**A**) P′, (**B**) −PET′, and (**C**) P′−PET′ for the WUS. Gray lines are observed anomalies, and red lines are analog anomalies. The yellow-shaded area represents the identified drought periods, same as Fig. 1. The vertical black line separates 1948–1999 (P1) and 2000–2022 (P2).

(Figs. 1A and 2C) compared to those during droughts in P1. Thus, climate change has not only intensified overall drying, as evidenced by the PET′ trend, but also greatly amplified drought severity from P1 to P2 (drought severity in table S5).

Drivers behind the unprecedented 2020–2022 drought over the WUS

The 2020–2022 drought over the WUS was unprecedented in the instrumental record (*3*). How have PET′ and P′ contributed to this drought? Figure 3A shows the evolution of this drought and the contribution of P′ and PET′ on a 31-day moving average timescale. This severe multiyear drought was initiated by an episode of strong precipitation deficit in March 2020, followed by frequent and persistent low precipitation periods extending from August 2020 to March 2022, except for intermittent episodes of heavy precipitation in November 2021 and January 2022. Although P′ magnitude remained larger than PET′ during most of the dry spells within this drought, high PET′ persisted throughout the entire time, even after precipitation deficits ceased in spring 2022. This continual presence of high PET′ prolonged the drought, and, over annual or longer timescales, PET′ eventually has a notably greater contribution than P′. When comparing the original observed anomalies to their analogs, the observed P′ can be mostly explained by its analog, with only a few minor exceptions. In contrast, the observed PET′ was consistently larger than its analog counterpart, especially during the warm season (April to October), providing evidence of the anthropogenic influence on these drought conditions.

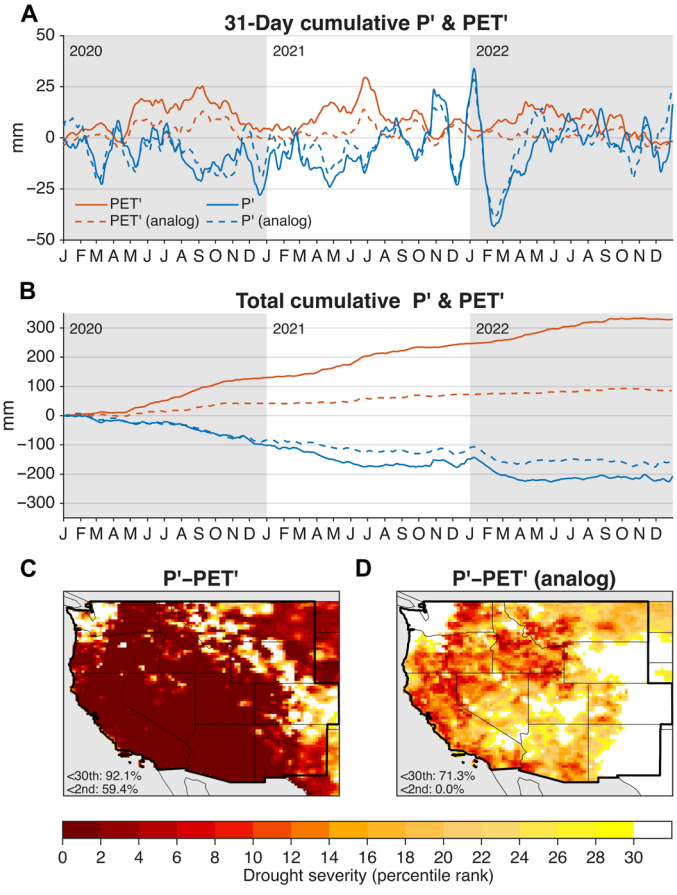

Fig. 3. The evolution of the 2020–2022 WUS drought and impacts of climate change. (**A**) Thirty-one-day moving average time series of P′ (blue) and PET′ (red) averaged over the WUS during 2020–2022. (**B**) Cumulative P′ and PET′ since 1 January 2020. In (A) and (B), P′−PET′ is represented by the distance between P′ and PET′ lines. (**C**) Drought severity map represented by percentile rank of 12-month P′−PET′ during the period of July 2020 to June 2021, where the percentiles are relative to the 1948–1999 P′−PET′ record (Materials and Methods); percentage WUS areas in drought condition (<30th percentile) and in exceptional drought condition (<2nd percentile) are also listed. (**D**) Circulation-contributed (analog) drought severity map; percentiles are relative to the 1948–1999 observed P′−PET′, same as (C). Complete percentile map for all components of the drought severity (observed, analog, and residual anomaly of P, −PET, and P−PET) are shown in fig. S8.

The total contribution of P′ and PET′ to the 2020–2022 WUS drought, along with their natural variability and anthropogenically influenced components, can be illustrated using the total cumulative values of these properties over the course of this drought (Fig. 3B). P′ was comparable to PET′ in magnitude in the early stage of the drought until the summer of 2021. Subsequently, cumulative PET′ exceeded P′ in magnitude and maintained the lead till the end of 2022. Over the 3-year period, although both P′ and PET′ have contributed to the cumulative P′−PET′, the relative contribution of PET′ (61%) notably exceeded that of P′ (39%), as indicated by the last data points of the cumulative P′ and PET′ time series in Fig. 3B. PET′ exceeding P′ in magnitude to such an extent has not been observed before the mid-2000s in our analysis period. Only about a quarter of the cumulative PET′, compared to about three-quarters of cumulative P′, can be explained by their analog values due to natural climate variability. As a result, less than half (44%) of the cumulative P′−PET′ can be attributed to natural climate variability, with the remaining larger share being driven by anthropogenic influences.

During the 12-month period of July 2020 to June 2021, at the peak of this multiyear drought with the lowest mean P′−PET′ (Figs. 1A and 2C), more than 90% of the WUS areas were in drought condition, i.e., local P′−PET′ falling below their local 30th percentile values based on the 1948–1999 distribution. Furthermore, more than half of the WUS experienced P′−PET′ below the second percentile values (Fig. 3C); this level of drought severity corresponds to "exceptional drought" according to the USDM's recommended percentile range for most drought indicators (*40*). Next, we investigate the spatial extent and severity of drought that would have occurred if anthropogenic climate change had not contributed to the development of this drought. Figure 3D shows that the analog P′−PET′ values, in the absence of anthropogenic influence, fell mostly within the 10th to 30th percentiles, based on the same historical distribution of observed P′−PET′. Continuing with the assumption that the differences between the observed and analog P′−PET′ represent the influences of anthropogenic forcing, Fig. 3D suggests that, without the influence of anthropogenic warming, although about three-quarters of the WUS areas would still be in drought condition, the areas corresponding to exceptional drought would be negligible (<0.1% of the WUS). In addition, while either P′ or PET′ alone can lead to widespread drought conditions (70 to 80% of the WUS; fig. S8, A and B), neither can solely lead to exceptional drought conditions over large areas.

Thus, while extreme precipitation deficit initiated the 2020–2022 WUS drought and dominated drought severity on a monthly timescale, warm surface temperatures and the resulting persistent high evaporative demand prolonged the drought and dominated its severity on an annual or longer timescale. While anthropogenic

warming influences or increased evaporative demand might not have been necessary for the widespread drought coverage during the peak of this event, they are crucial factors enabling this drought to reach "exceptional" severity levels.

The impact of high greenhouse gas emissions on future droughts over the WUS

Does the 2020–2022 WUS drought represent an exceptional anomaly or a future "new norm" for the region? We explore future P′−PET′ trends using the multi-model all-forcing historical simulations provided by the Coupled Model Intercomparison Project Phase 6 (CMIP6) and the future projections under the Shared Socioeconomic Pathway 5-8.5 (SSP5-8.5) scenario (*49*). Data from these two experiments are combined to form a continuous record from 1948 to 2100 and bias corrected using the quantile delta mapping (QDM) approach (*50*) (Materials and Methods and fig. S9). A total of 30 climate models and more than 300 ensemble members are used in this study; model names and the number of ensemble members for each model are listed in table S6. It is important to note that the SSP5-8.5 scenario is the highest emission scenario assuming fossil-fueled rapid economic growth (SSP5) with a high radiative forcing level by 2100 (8.5 W/m^2) and may not be the most likely future.

Figure 4A shows that these CMIP6 model simulations generally capture the observed P′−PET′ trend over the WUS during 1948–2022, supporting the hypothesis that the trend is anthropogenically forced and consistent with our flow analog analysis shown above. Despite the uncertainty of the individual models, particularly regarding the direction of future P′ trend and the extent of the positive PET′ trend (fig. S10), the CMIP6 ensemble means project a steady decrease in P′−PET′ due to increasing PET′, consistent with the decreasing trend found in modeled surface soil moisture (fig. S11A). This suggests a shift toward a more arid and warmer climate over the WUS in the future. Furthermore, the models also predict a larger range of variability in P′−PET′. This heightened variability is driven by increased fluctuations in both PET′ and P′, although the increase in variability is more pronounced for PET′ (figs. S12 and S13). The projected future increases in PET′ and P′, with larger variability than in the past, heighten the potential for more severe droughts and floods. On the basis of our analysis of the modeled P′−PET′ distribution for both historical and future periods, droughts as severe as those experienced during 2020–2022 are projected to become increasingly frequent. By analyzing the area under the P′−PET′ distribution curve (fig. S13C) to the left of the observed minimum P′−PET′ value (July 2020 to June 2021), we calculate the exceedance probability for future droughts to reach or exceed this level of severity. Our findings indicate that, according to model simulations, the exceedance probability for such events will increase from being very rare (0.08% or 1-in-1300-year) in the recent 2000–2022 (P2) period to 1.6% (1-in-63-year) by 2040–2060 and 17% (1-in-6-year) by 2080–2100 over the WUS. Detailed statistics of the exceedance

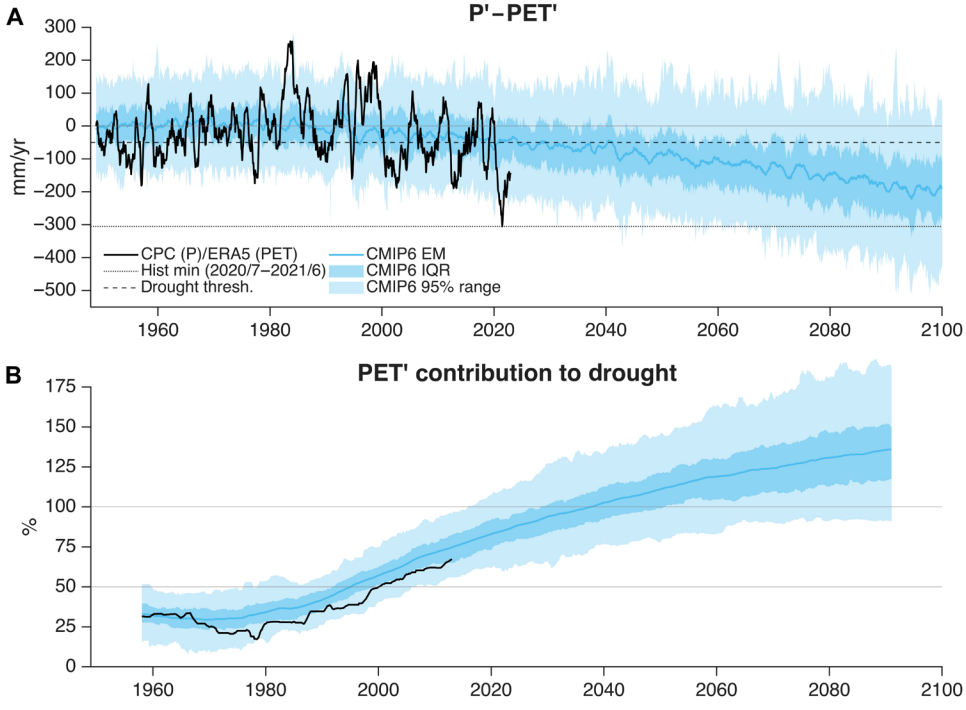

Fig. 4. Comparison between observed and CMIP6 modeled drought severity and evolution of PET′ contribution. (**A**) Observed (black) and CMIP6 (blue) 12-month moving cumulative time series of P′−PET′ averaged over the WUS. (**B**) PET′ contribution to drought severity, defined as the magnitude of −PET′/(P′−PET′) averaged during drought periods (12-month P′−PET′ < 30th percentile) for both observations and CMIP6 models. To acquire a smooth PET′ contribution time series, it is averaged during drought periods in a sliding 20-year window centered at the time of interest (e.g., the value for 1958 represents droughts during 1948–1967). Black and blue lines represent the observation and CMIP6 multi-model ensemble mean, respectively. The dark blue– and light blue–shaded areas represent the range of climate variability as depicted by the interquartile range (IQR) and 95% range of results from individual model realizations, respectively. In (A), the horizontal dashed line represents the 30th percentile P′−PET′ threshold value for drought, and the horizontal dotted line represents the P′−PET′ during 2020/7–2021/6, the peak 12-month drought severity during the 2020–2022 WUS drought. All anomalies are relative to their corresponding 1948–1999 climatologies.

probabilities for various periods, based on both observations and models, are listed in table S7.

Figure 4B compares PET′ contribution to drought severity averaged in 20-year moving windows between observations and CMIP6. The observed PET′ contribution was initially about 30% and then experienced a slight decrease from the 1950s to the 1980s, attributed to "global dimming" driven primarily by increased aerosols and cloud cover according to previous studies (*51*), which reduced surface shortwave radiation and subsequently lowered PET. Since then, the PET′ contribution has climbed steadily and reached the milestone of 50% around 2000, marking the turning point from precipitation deficit dominance to high evaporative demand dominance of droughts in the WUS. The time series of the CMIP6 ensemble mean PET′ contribution generally follows the observed increasing trend, although it reached 50% in the mid-1990s, earlier than that observed mainly because models overestimate PET′ magnitude during drought periods in P1 (fig. S14B). In addition, this discrepancy could also be influenced by errors in how the models simulate the response to aerosol forcing and the subsequent recovery after 1970s, which may have affected the timing of changes in PET′ contribution. The CMIP6 models project that PET′ contribution will continue to increase. Because of the strong increase in future PET′, weak to moderate droughts may occur with positive P′ (fig. S14A). These weaker droughts generally show larger PET′ contributions compared to stronger droughts (fig. S15, A and C), which are typically associated with negative P′. Such an effect might potentially hinder an ending of drought conditions. By 2040–2060, weaker droughts with positive P′ will account for about half of the total future drought events (fig. S14A), leading to more than 100% PET′ contribution to drought severity, i.e., $-PET'/(P'-PET') > 100\%$. In addition, the projected increase in precipitation (figs. S12A and S13A) will weaken precipitation deficits during droughts. Overall, the combined effects of these increases in P′ and PET′ lead to the projected PET′ contribution to drought severity exceeding 100% in the future. In addition, this anticipated increase in PET′ contribution to drought severity does not solely stem from the average warming trend but also from the increase in PET variability. In both observation and models, the distribution of PET′ has been narrower than that of P′ in the historical period, but their spreads are projected to become comparable by the end of the 21st century (figs. S12 and S13).

DISCUSSION

This study has uncovered that rising temperatures and the resulting high evaporative demand have surpassed precipitation deficit as the dominant drought driver around the year 2000 in the WUS. This change cannot be explained by natural climate variability and is mainly caused by warming due to anthropogenic forcing. This drought regime shift has led to increased drought severity and coverage since the turn of the 21st century, marking the beginning of a new era where WUS droughts are increasingly driven by evaporative demand rather than precipitation deficits. The 2020–2022 WUS extreme drought exemplifies this new paradigm. While this exceptional drought was initiated by record-low precipitation during its first year and a half, high surface temperature persisted afterward for another year. High temperatures contributed more (61%) to the drought's severity than precipitation deficit (39%), and the drought lasted longer than that expected from a traditional precipitation deficit–dominated drought. More than half of the WUS experienced exceptional drought (P′−PET′ below the second percentile), far exceeding the would-be drought severity (10th to 30th percentiles) without climate change impact. The 2020–2022 drought is likely a presage of future drought patterns in the region.

Climate model simulations show a similar, albeit earlier, shift in drought drivers. The early bias is likely due to the lack of realistic decadal climate variability in the ensemble mean and model biases. The degree of aridification and intensification of droughts in the region depends on the extent of anthropogenic warming. Under an energy-intensive, fossil-fueled economic development scenario (SSP5-8.5), the WUS is projected to become more arid and drought prone than has been hitherto observed. By the mid-21st century, more than half of the future droughts would occur even with heavier precipitation than its climatological values in the recent past (1948–1999). Droughts like the 2020–2022 event, a rare occurrence in the current climate—equivalent to a one-in-more-than-a-thousand-year event—are projected to become more frequent, equivalent to a 1-in-60-year event by the mid-21st century and a 1-in-6-year event by the late-21st century.

One can glimpse the impacts of temperature-dominated droughts through the lens of the 2020–2022 WUS drought. This drought was associated with high VPD, which contributes to the occurrence of wildfires or intensifies them, further exacerbating drought impacts (*3*). In 2020 alone, the combined cost of drought and wildfire reached up to $23 billion in the southwestern US, more than an order of magnitude higher than the cost of drought alone (*3*). The cascading economic impacts, such as supply chain disruptions, and long-term effects on public health, particularly from smoke and heat stress, are likely on the order of hundreds of billions (*52*). As surface temperature increases under the fossil-fueled economic development scenario, drought can occur without precipitation deficits. In addition, drought will become more intense, more frequent, and longer-lasting. These observed and projected changes over the WUS highlight the importance of new drought monitoring and management strategies to effectively manage and support long-term societal resilience to droughts in a changing climate, and the urgency to control greenhouse gas emissions to avoid a much more arid and drought-prone future over the WUS than it has experienced in the recent history and possibly in the last millennium.

Our findings, while consistent with extensive research demonstrating the growing contribution of temperature-driven evaporative demand to drought (*3*, *5*, *6*, *15*–*21*), differ from previous studies (*22*–*24*) that found that precipitation deficit remained the primary drought driver. The differences arise from several factors and should not be simply viewed as contradictory. For example, earlier studies (*23*) may not include the recent period when PET's impact surged. In addition, studies (*22*, *25*, *32*) using CRU data may underestimate PET impact, as PET data from CRU are calculated with synthetic vapor pressure (VP) derived from daily minimum temperature as a proxy for dew point temperature, which can result in an unrealistic wetting trend due to anthropogenic warming, especially for semi-arid to arid regions (*53*). In particular, a more recent study (*33*) has reported drying trends in the southwestern US based on ERA5 VP data, which has been validated with in situ measurements. Our analysis (Supplementary Text and figs. S2 and S3) further supports that the discrepancies in PET between ERA5 and CRU datasets primarily arise in the southwestern US and are mainly due to their opposite VP trends.

There are limitations in our analysis. The analysis period of 75 years may not cover the full range of the natural climate variability, especially

compared to that suggested by paleoclimate records (*7*). While the FAO-56 Penman-Monteith (PM) equation that we used is considered the best practice for calculating PET due to its physical basis and reliability validated by numerous studies (*54*–*56*), it assumes time-invariant surface resistance to avoid the inherent complexity of determining the stomatal and atmospheric conductance and to foster standardization and consistency in climatic research (*57*, *58*). Such an assumption may not hold with changes in land surface and vegetation cover in a changing climate; future research could explore the impact of incorporating dynamic surface conductance in PET calculations, as demonstrated by (*59*). Over the long term, PET is largely influenced by temperature, yet surface wind speed also plays a role. Although model projections of surface wind generally carry higher uncertainty compared to temperature (*60*), our model results indicate a slightly decreasing trend in wind speed (fig. S9), which has lowered the PET trend compared to calculations with wind climatology of the 20th century. As a drought index, P′−PET′ tends to have greater amplitudes and variations than soil moisture anomalies over the moisture-limited regions (fig. S11), especially during droughts. Furthermore, the impacts of PET′ on vegetation and surface hydrology in the future cannot be simply extrapolated from today's climate, in part due to plants' physiological responses to elevated CO_2 (*61*). In our observation-based circulation analog analysis, the analog approach might overestimate natural climate variability because it assumes that the positive trend in circulation-induced PET′ is solely due to natural climate variability (*29*); some studies have suggested that anthropogenic forcing contributes to an increased frequency of ridging patterns over the WUS associated with high PET or VPD (*62*, *63*), although the potential impact of climate change on circulation changes remains debated (*64*, *65*). The land-surface and atmospheric thermodynamic feedbacks to the natural atmospheric circulation anomalies may be stronger in a warmer, drier climate with elevated CO_2 concentration (*66*). These potential effects on PET′ and P′ are not captured by our flow analog analysis that relies on historical data. Last, while SSP5-8.5 aligns with historical cumulative CO_2 emissions (*67*), it represents only one potential future characterized by very high emissions. However, these limitations are unlikely to alter our main conclusions qualitatively.

MATERIALS AND METHODS

Observation-based data

The precipitation dataset used in this study is the National Oceanic and Atmospheric Administration (NOAA) CPC Unified Gauge-Based Analysis of Daily Precipitation over CONUS (*35*), provided by the NOAA Physical Sciences Laboratory, from their website at https://psl.noaa.gov/data/gridded/data.unified.daily.conus.html. This dataset has a spatial resolution of 0.25° × 0.25° and a temporal coverage from 1948 to the present. This study uses data during 1948–2022.

The fifth-generation European Centre for Medium-Range Weather Forecasts (ECMWF) atmospheric reanalysis of the global climate (ERA5) (*34*) data are retrieved from the Copernicus Climate Change Service Climate Data Store (https://cds.climate.copernicus.eu). This global reanalysis dataset covers the period from 1940 to the present and has a native spatial resolution of 0.25° × 0.25°. We use this dataset for observed PET calculation and characterization of mid-tropospheric circulation, with data during 1948–2022 to match the CPC dataset described above. Variables used from the ERA5 include 2-m temperature, 2-m dew point temperature, 10-m *u*-component of wind, 10-m *v*-component of wind, mean surface downward short-wave radiation flux, forecast albedo, and 500-hPa geopotential (Z500). For Z500, 6-hourly data at 1° × 1° resolution are retrieved. Similar to (*29*), the daily global area-weighted mean Z500 is subtracted from the original daily Z500 data at each grid point (*68*, *69*) to remove the large-scale increase in Z500 due to the expansion of the atmospheric column as global surface temperature increases (*62*). For other variables, hourly data at 0.25° × 0.25° resolution are retrieved and averaged to daily value, except for temperature and wind. For hourly temperature, daily maximum and minimum values are calculated. Hourly *u*- and *v*-components of wind are used to calculate wind speed and then averaged to daily values.

Climate model data and bias correction

Monthly climate model outputs, specifically precipitation flux (pr), maximum and minimum near-surface air temperature (tasmax and tasmin), near-surface relative humidity (hurs), near-surface wind speed (sfcWind), and surface downwelling shortwave radiation (rsds), are obtained from 30 climate models participating in the sixth phase of the Climate Model Intercomparison Project. The historical simulations spanning 1850–2014 are combined with SSP5-8.5 projections for 2015–2100 to produce a continuous record. For each model, only those realizations that are common to both historical simulations and SSP5-8.5 projections are used for P and PET analysis. Details about the specific models and the number of ensemble numbers used are listed in table S6. Data of all models are bilinearly interpolated to a common spatial resolution of 1° × 1° to ensure consistency in the analysis and facilitate the computation of the ensemble mean. When calculating the multi-model ensemble mean, we first average all ensemble members within each model and then average the results across all models. For ensemble spread metrics, such as SD, percentiles, and probability density functions, each ensemble member is assigned a weight inversely proportional to the number of ensemble members in its model. This ensures that each model contributes equally to our analysis, regardless of the number of ensemble members it has.

Although climate model simulation and projections are important tools for assessing climate impact, it is well-known that there are systematic biases between climate model output and observations. Model biases can manifest as consistent overestimation or underestimation of certain climate variables, including their mean, variability, extremes, and distribution inconsistency compared to observations. To address these biases, bias correction methods are developed to statistically adjust model outputs with reference to observation data. Past studies have shown that projections of aridity and drought can exhibit large discrepancies between raw model output and bias-corrected output (*70*). In this study, we use the QDM technique (*50*) for bias correction. QDM corrects the model biases by adjusting the quantiles of modeled data to match observed data quantiles while preserving the model's projected climate change signal (*71*). The code and data that we used to perform QDM are deposited at https://zenodo.org/doi/10.5281/zenodo.13836244. All datasets are regridded to a 1° × 1° resolution before bias correction to address the mismatch in spatial resolution between the observations (e.g., ERA5 and CPC) and the CMIP6 climate models. Bias correction is conducted at the grid scale before averaging the results over the WUS. For precipitation, the multiplicative delta method is used, while the additive delta method is used for other variables. The reference dataset for precipitation and other input variables for PET calculation is CPC and ERA5, respectively, with a consistent reference period of 1948–1999 for all variables. The comparison between raw climate model output

and the bias-corrected data, in terms of the WUS mean time series of all model variables mentioned above, is shown in fig. S9. Apart from this comparison, we only report results based on the QDM bias-corrected data.

Calculation of PET

PET quantifies the maximum amount of actual evapotranspiration under reference land surface condition when there is no limit for water availability. PET is largely determined by temperature, though it can also be influenced by humidity, wind, surface radiation, etc. Because PET represents surface moisture loss to the atmosphere, a higher PET value signifies a more severe drought. PET can be estimated by many different approaches. Simpler methods such as Thornthwaite (*72*) usually overestimate the PET magnitude and trend (*73*). Here, we used the FAO-56 PM equation, a physically based method recommended by the Food and Agriculture Organization (FAO) (*54*) as well as many previous studies (*55*, *56*). The PM equation requires input variables including maximum temperature, minimum temperature, humidity (e.g., dew point temperature or relative humidity), wind speed, and incoming shortwave radiation.

The original PM equation assumes a homogeneous surface albedo of 0.23; here, to better account for the spatial variation, we used the 1948–1999 climatological mean surface forecast albedo from ERA5 for each grid point. PET data are first calculated at a daily scale and then aggregated to a monthly scale. For the flow analog analysis (Figs. 2 and 3), the daily PET anomaly (PET′) is used as input. When showing observed PET′ in other figures, the aggregated monthly PET′ is used. Our additional analysis in fig. S1 also indicates that temperature is the most influential factor for WUS PET, with VP (derived from dew point) as the second. Only considering the variabilities of temperature and VP while using climatology for other inputs can still allow us to account for 94% of the variance observed in the original calculation. Excluding either temperature or VP results in a substantial reduction in the representation of PET variability and its long-term trend. We also compared the PET′ calculated with ERA5 data and that with the Global Surface Summary of the Day (GSOD) data to confirm the ERA5 PET′ well represents the station observation (Supplementary Text and fig. S16).

For CMIP6 models, PET′ is only calculated at a monthly scale using monthly tasmax, tasmin, hurs, sfcWind, and rsds as inputs to the PM equation. These input variables are individually bias corrected before being used in the PM equation to calculate bias-corrected PET. An exception is made for hurs, which is first converted to VP and then bias corrected (*74*); we made this adjustment because relative humidity (hurs) is not an absolute measure of atmospheric humidity and can be considerably influenced by temperature as well, and we have dew point temperature in ERA5 instead of relative humidity. For simplicity, we use the ERA5 1948–1999 monthly climatological surface albedo, consistent with the observed PET. Note that the PM equation with monthly inputs differs slightly from that with daily inputs (e.g., soil heat flux G cannot be omitted and is estimated with temperature changes). It is expected that the aggregated monthly PET′ from daily inputs and PET′ calculated directly from monthly inputs may not be exactly the same. Nevertheless, our additional analysis shows that, at least for the period of 1948–2022 and averaged over the WUS, observed PET′ calculated with daily and monthly ERA5 inputs (whether at the original 0.25° × 0.25° resolution or the reduced 1° × 1° resolution) are highly consistent and significantly correlated (fig. S17). In addition, considering the large volume of CMIP6 data, it is both reasonable and efficient to perform the comparison between observed and modeled PET′ at a monthly scale.

Calculation of anomalies

Daily anomalies of P (P′) and PET (PET′) are calculated as their respective departures from the 1948–1999 daily climatology and then aggregated to monthly values. Standardized anomalies are used only with circulation data (Z500) or when comparing P′−PET′ to soil moisture and other drought indices, as these variables have different units. The daily climatological mean and SD for a specific Julian day are computed using daily samples within a 31-day calendar window centered on that day (*29*, *75*); for example, the climatology for 1 January is calculated using daily data from 17 December to 16 January during 1948–1999 (31 days/year × 52 years = 1612 days). For monthly data (e.g., soil moisture and CMIP6 model data), climatology is directly calculated for each month during the same 1948–1999 period; however, for fig. S4, where we compare P′−PET′, soil moisture, and other drought indices, we use the 1980–2010 period as the climatological baseline to calculate standardized anomalies when all the datasets are available.

Drought severity, drought coverage, and contributions of P and PET

In this study, drought severity is defined as the 12-month cumulative P′−PET′ for either the area average for the WUS or for individual grid points. For each 12-month period, the contributions of P′ and PET′ to the drought severity are defined as their respective ratio: P′/(P′−PET′) for P′, and −PET′/(P′−PET′) for PET′.

For most analyses in this study, the term "drought period" (yellow-shaded area in Figs. 1, A and B, and 2) refers to any 12-month period when the WUS mean P′−PET′ falls below its 30th percentile value. This threshold is recommended by the USDM from their "Drought classification – percentile range for most indicators" and is comparable to their "D0 – abnormally dry" category (*40*) (see also https://droughtmonitor.unl.edu/About/AbouttheData/DroughtClassification.aspx). However, it is important to note that the actual USDM product is not based solely on percentile range of a single drought index; rather, it involves assessments of a wide range of indicators and expert guidance. The percentile threshold is based on 12-month P′−PET′ values during 1948–1999 (12-month windows from 1948/1–1948/12, 1948/2–1949/1,…, to 1999/1–1999/12, resulting in a total of 613 samples) and is calculated using the "prctile" function in MATLAB. In Fig. 1 (C and D), where we show the spatial distribution of average PET contribution to drought severity for each grid point during P1 and P2, the drought period is defined for each grid point locally using the same approach. In addition, when calculating the average P or PET contribution to drought severity in P1 or P2 (Fig. 1, C and D, and table S3) to be consistent with the "12-month" timescale, we first calculate P or PET contributions across all 12-month periods identified as drought periods within P1 or P2 and then average them to get the mean P or PET contribution to drought severity in P1 or P2.

To determine drought coverage at any 12-month period, we first identify the "drought" status of each grid point using their local P′−PET′ values and then calculate the area covered by these grid points, taking into account the area weighting of grid points (i.e., cosine latitude). To further determine the contribution of P′ to drought coverage, we first set PET′ to zero and identify grid points where P′ alone can cause P′−PET′ to fall below the same local 30th percentile threshold values as determined in the reference period

of 1948–1999. The proportion of these grid points' area to the original total drought coverage, as previously determined by the actual P′−PET′, is used to quantify P contribution to drought coverage. PET contribution is quantified in a similar way by setting P′ to zero. Note that the contributions of P and PET to drought coverage do not necessarily add up to 100% as they do for drought severity because the definition of drought coverage does not follow a simple additive form like drought severity. Determination of drought coverage depends on the "drought status" of each grid point, where some grid points may be in drought due to a combination of both factors.

Quantifying circulation contribution: Ensemble constructed flow analog

The observation-based flow analog (or circulation analog) method is widely used to quantify circulation contribution to surface meteorological variables such as temperature, precipitation, and VPD (*43*, *76*–*78*). Our study uses the ensemble constructed flow analog approach (*29*), a variant that uses multiple analog schemes to provide a more robust estimation of circulation contribution and quantify the uncertainties. Applying this technique, we determine circulation-induced P or PET anomalies, or simply termed analog P or PET anomalies, at a daily scale using historical information from days with similar circulation conditions. Similar to how we process the original observed anomalies, these analog anomalies are then aggregated over the moving 12-month windows to represent the influence of circulation change or internal variability on drought conditions.

Several data preprocessing procedures are implemented before the analog analysis. For circulation data, we subtract the daily global area-weighted mean Z500 from the original Z500 data to remove trends (*68*, *69*) due to warming-induced thermal expansion effect (*62*). There are other detrending approaches used in the literature, such as local linear detrending or high-pass filtering, which assumes the forced circulation trend is smooth and additive. We do not use local detrending because, at a decadal scale with a relatively short observation record, circulation trends can result from both thermal expansion and internal variability (e.g., certain circulation types becoming more frequent due to phase shift of climate modes). Local detrending would eliminate these signals altogether, whereas our approach preserves local circulation changes not related to thermal expansion. However, this approach does not remove any potential anthropogenically driven changes in circulation patterns (*79*). For P and PET data, we apply a locally weighted scatterplot smoother with a span value of 0.5 and a first-degree polynomial model. This fitted low-frequency trend, which approximates anthropogenic influence, is subtracted from the P and PET data. In addition, to mitigate high-frequency synoptical noises, a simple 5-day moving average filter is applied to Z500, P, and PET data that are used as input for the analog analysis.

The main steps for the ensemble constructed flow analog include the following:

1) Analog selection: For any target day j, we select N analog days ($i = 1, 2, \ldots, N$) with similar circulation by minimizing the distance function between the standardized anomaly of Z500 (Z500′) field of the target day j and those of the analog days i. The analog day selection is limited to a 61-day window centered on the target calendar day, drawn from the reference period 1948–1999 (excluding the target year).

2) Circulation regression: The Z500′ patterns from the N analog days are used to linearly regress against the target day Z500′ pattern, i.e., $Z500'_j = \sum_{i=1}^{N} \left(a \cdot Z500'_i\right)$. After solving for coefficient a_i ($i = 1, 2, \ldots, N$), the fitted field $\sum_{i=1}^{N} \left(a_i \cdot Z500'_i\right)$ is the "constructed analog" Z500′ pattern, which closely resembles the target day $Z500'_j$.

3) Calculation of analog and residual components: The coefficients a_i are applied to P′ or PET′ of the analog days to calculate the analog P′ or PET′, i.e., $P'_{j-\mathrm{ANA}} = \sum_{i=1}^{N} a_i P'_i$, which represents the contribution from circulation or internal variability. The residual, $P'_{j-\mathrm{RES}} = P'_j - P'_{j-\mathrm{ANA}}$, captures the thermodynamic influences.

4) Ensemble schemes: The above three steps are repeated for three distance functions (Euclidean distance, Pearson's correlation, and Spearman's rank correlation), three geographic domains for Z500′ input (160°W to 80°W, 20°N to 60°N; 150°W to 90°W, 25°N to 55°N; and 140°W to 100°W, 30°N to 50°N), and five nonoverlapping daily subsets (days 1, 6, 11, …; days 2, 7, 12, …; etc.). Sampling from one of the five daily subsets avoids selecting consecutive days from the same weather event. The mean of the resulting 45 ($3 \times 3 \times 5$) estimates serves as the final analog value for P′ or PET′, and the interquartile range of them is used to quantify the uncertainty. In addition, for precipitation, if the calculated $P'_{j-\mathrm{ANA}}$ is below the negative climatological value $-\overline{P_j}$, then we assign it the value of $-\overline{P_j}$, so that the total analog precipitation value, $P_{j-\mathrm{ANA}} = \overline{P_j} + P'_{j-\mathrm{ANA}}$, remains nonnegative.

Other statistical analysis

Area weighting (using cosine latitude as the weight for each grid point) is applied across all analyses in this study whenever the analysis is for the WUS overall instead of individual grid points. When we compare the spatial distribution of drought with or without the anthropogenic influences during 2020/7–2021/6, the peak of the 2020–2022 WUS drought (Fig. 3, C and D), we show percentile rank instead of the original values of the 12-month P′−PET′ to provide a more straightforward understanding of drought severity and facilitate comparisons across different regions. These percentile ranks of the 12-month moving cumulative P′−PET′, or simply termed percentile P′−PET′, are calculated for each grid point using the "invprctile" function in MATLAB (www.mathworks.com/matlabcentral/fileexchange/41131-inverse-percentiles-of-a-sample). This calculation is based on 12-month P′−PET′ data from the reference period 1948–1999, which includes $n = 613$ samples from the 12-month moving windows (1948/1–1948/2, 1948/2–1949/1, …, 1999/1–1999/12). To calculate the percentile P′−PET′ of a target period (e.g., 2020/7–2021/6), the P′−PET′ values from the n reference samples are first sorted in ascending order. Then, the position i of the target P′−PET′ in the sorted list is determined. Last, the percentile P′−PET′ of the target period is calculated as $(i - 0.5)/n$.

When assessing the significance (P value) of temporal correlation (figs. S1 to S3, S16, and S17 and table S1), we follow (*80*) to adjust the effective sample size (degrees of freedom) to account for the autocorrelation present in the time series data, avoiding overestimation of the correlation's significance. To assess the significance of the increase in PET contribution from P1 to P2 at WUS grid points (Fig. 1E), we apply the FDR controlling criterion (*44*) using the MATLAB function "fdr_bh" (www.mathworks.com/matlabcentral/fileexchange/27418-fdr_bh). The FDR method reduces the likelihood of false positives by adjusting for multiple comparisons, which is important given the potential spatial autocorrelation in the data.

We use a Monte Carlo permutation test (*75*) to evaluate whether the contribution of P′ or PET′ to drought severity or coverage has significantly changed from P1 to P2 and whether PET′ contribution to drought severity or coverage is significantly different than P′ contribution in either P1 or P2. We begin by randomly permuting the order of years in P and PET data and then recalculating the 30th percentile P′−PET′ threshold for drought using the permuted 1948–1999 data. Next, we recalculate the contributions of PET′ or P′ to drought severity and coverage. This process is repeated 10,000 times. Last, for example, to test the null hypothesis that PET contribution is no larger than P contribution to drought severity in P2 (one-sided test), we compare the original difference between PET and P contributions to drought severity in P2; if this difference is larger than 96% of the permuted difference, then it is considered significant at the 0.05 level, with the *P* value being 0.04. The one-sided test is used as we focus on directional hypotheses. As discussed in Introduction, previous studies have consistently shown an increasing PET trend in many regions due to global warming which intensified droughts; given this established direction of change, we are specifically testing whether PET′ has become a more dominant factor in drought compared to P′ and whether drought severity/coverage has intensified/expanded. The results of all null hypotheses tested and their significance levels are shown in tables S2 and S3.

Supplementary Materials

This PDF file includes:

Supplementary Text
Figs. S1 to S17
Tables S1 to S7
References

REFERENCES AND NOTES

1. N. S. Christensen, A. W. Wood, N. Voisin, D. P. Lettenmaier, R. N. Palmer, The effects of climate change on the hydrology and water resources of the Colorado River basin. *Clim. Change* **62**, 337–363 (2004).
2. M. Xiao, B. Udall, D. P. Lettenmaier, On the causes of declining Colorado River streamflows. *Water Resour. Res.* **54**, 6739–6756 (2018).
3. J. S. Mankin, I. Simpson, A. Hoell, R. Fu, J. Lisonbee, A. Sheffield, D. Barrie, "NOAA Drought Task Force Report on the 2020–2021 Southwestern U.S. Drought" (NOAA Drought Task Force, MAPP, and NIDIS, 2021).
4. J. Lisonbee, E. Ossowski, M. Muth, V. Deheza, A. Sheffield, Preparing for long-term drought and aridification. *B. Am. Meteorol. Soc.* **103**, E821–E827 (2022).
5. A. P. Williams, E. R. Cook, J. E. Smerdon, B. I. Cook, J. T. Abatzoglou, K. Bolles, S. H. Baek, A. M. Badger, B. Livneh, Large contribution from anthropogenic warming to an emerging North American megadrought. *Science* **368**, 314–318 (2020).
6. A. P. Williams, B. I. Cook, J. E. Smerdon, Rapid intensification of the emerging southwestern North American megadrought in 2020-2021. *Nat. Clim. Change* **12**, 232–234 (2022).
7. B. I. Cook, J. E. Smerdon, E. R. Cook, A. P. Williams, K. J. Anchukaitis, J. S. Mankin, K. Allen, L. Andreu-Hayles, T. R. Ault, S. Belmecheri, S. Coats, B. Coulthard, B. Fosu, P. Grierson, D. Griffin, D. A. Herrera, M. Ionita, F. Lehner, C. Leland, K. Marvel, M. S. Morales, V. Mishra, J. Ngoma, H. T. T. Nguyen, A. O'Donnell, J. Palmer, M. P. Rao, M. Rodriguez-Caton, R. Seager, D. W. Stahle, S. Stevenson, U. K. Thapa, A. M. Varuolo-Clarke, E. K. Wise, Megadroughts in the Common Era and the Anthropocene. *Nat. Rev. Earth Env.* **3**, 741–757 (2022).
8. S. Stevenson, S. Coats, D. Touma, J. Cole, F. Lehner, J. Fasullo, B. Otto-Bliesner, Twenty-first century hydroclimate: A continually changing baseline, with more frequent extremes. *Proc. Natl. Acad. Sci. U.S.A.* **119**, e2108124119 (2022).
9. T. R. Ault, J. S. Mankin, B. I. Cook, J. E. Smerdon, Relative impacts of mitigation, temperature, and precipitation on 21st-century megadrought risk in the American Southwest. *Sci. Adv.* **2**, e1600873 (2016).
10. T. R. Ault, J. E. Cole, J. T. Overpeck, G. T. Pederson, D. M. Meko, Assessing the risk of persistent drought using climate model simulations and paleoclimate data. *J. Climate* **27**, 7529–7549 (2014).
11. M. Sugg, J. Runkle, R. Leeper, H. Bagli, A. Golden, L. H. Handwerger, T. Magee, C. Moreno, R. Reed-Kelly, M. Taylor, S. Woolard, A scoping review of drought impacts on health and society in North America. *Clim. Change* **162**, 1177–1195 (2020).
12. S. M. Vicente-Serrano, D. Peña-Angulo, S. Beguería, F. Domínguez-Castro, M. Tomás-Burguera, I. Noguera, L. Gimeno-Sotelo, A. El Kenawy, Global drought trends and future projections. *Philos. T. R. Soc. A* **380**, 20210285 (2022).
13. A. G. Dai, Drought under global warming: A review. *WIREs Clim. Change* **2**, 45–65 (2011).
14. D. G. Miralles, P. Gentine, S. I. Seneviratne, A. J. Teuling, Land-atmospheric feedbacks during droughts and heatwaves: State of the science and current challenges. *Ann. N. Y. Acad. Sci.* **1436**, 19–35 (2019).
15. B. Udall, J. Overpeck, The twenty-first century Colorado River hot drought and implications for the future. *Water Resour. Res.* **53**, 2404–2418 (2017).
16. D. R. Easterling, T. W. R. Wallis, J. H. Lawrimore, R. R. Heim, Effects of temperature and precipitation trends on US drought. *Geophys. Res. Lett.* **34**, 10.1029/2007GL031541 (2007).
17. S. Z. Huang, G. Y. Leng, Q. Huang, Y. Y. Xie, S. Y. Liu, E. H. Meng, P. Li, The asymmetric impact of global warming on US drought types and distributions in a large ensemble of 97 hydro-climatic simulations. *Sci. Rep.* **7**, 5891 (2017).
18. D. S. Gutzler, T. O. Robbins, Climate variability and projected change in the western United States: Regional downscaling and drought statistics. *Clim. Dynam.* **37**, 835–849 (2011).
19. N. S. Diffenbaugh, D. L. Swain, D. Touma, Anthropogenic warming has increased drought risk in California. *Proc. Natl. Acad. Sci. U.S.A.* **112**, 3931–3936 (2015).
20. M. Osman, B. F. Zaitchik, N. S. Winstead, Cascading drought-heat dynamics during the 2021 Southwest United States heatwave. *Geophys. Res. Lett.* **49**, e2022GL099265 (2022).
21. C. A. Woodhouse, D. M. Meko, G. M. MacDonald, D. W. Stahle, E. R. Cooke, A 1,200-year perspective of 21st century drought in southwestern North America. *Proc. Natl. Acad. Sci. U.S.A.* **107**, 21283–21288 (2010).
22. R. Wang, L. H. Li, L. J. Chen, L. Ning, L. W. Yuan, G. N. Lü, Respective contributions of precipitation and potential evapotranspiration to long-term changes in global drought duration and intensity. *Int. J. Climatol.* **42**, 10126–10137 (2022).
23. D. L. Ficklin, J. T. Maxwell, S. L. Letsinger, H. Gholizadeh, A climatic deconstruction of recent drought trends in the United States. *Environ. Res. Lett.* **10**, 044009 (2015).
24. L. F. Luo, D. Apps, S. Arcand, H. T. Xu, M. Pan, M. Hoerling, Contribution of temperature and precipitation anomalies to the California drought during 2012-2015. *Geophys. Res. Lett.* **44**, 3184–3192 (2017).
25. N. Pan, S. Wang, Y. X. Liu, Y. Li, F. Xue, F. L. Wei, H. P. Yu, B. J. Fu, Rapid increase of potential evapotranspiration weakens the effect of precipitation on aridity in global drylands. *J. Arid Environ.* **186**, 104414 (2021).
26. J. T. Martin, G. T. Pederson, C. A. Woodhouse, E. R. Cook, G. J. McCabe, K. J. Anchukaitis, E. K. Wise, P. J. Erger, L. Dolan, M. McGuire, S. Gangopadhyay, K. J. Chase, J. S. Littell, S. T. Gray, S. S. George, J. M. Friedman, D. J. Sauchyn, J. M. St-Jacques, J. King, Increased drought severity tracks warming in the United States' largest river basin. *Proc. Natl. Acad. Sci. U.S.A.* **117**, 11328–11336 (2020).
27. F. Chiang, O. Mazdiyasni, A. AghaKouchak, Evidence of anthropogenic impacts on global drought frequency, duration, and intensity. *Nat. Commun.* **12**, 2754 (2021).
28. R. Fu, C. J. Wang, D. J. Ma, H. F. Gu, Q. Y. Xie, G. X. Liu, G. F. Yin, Attribution of air temperature and precipitation to the future global drought events. *Environ. Res. Commun.* **5**, 061005 (2023).
29. Y. Z. Zhuang, R. Fu, B. D. Santer, R. E. Dickinson, A. Hall, Quantifying contributions of natural variability and anthropogenic forcings on increased fire weather risk over the western United States. *Proc. Natl. Acad. Sci. U.S.A.* **118**, e2111875118 (2021).
30. S. M. Vicente-Serrano, S. Beguería, J. I. López-Moreno, A multiscalar drought index sensitive to global warming: The standardized precipitation evapotranspiration index. *J. Climate* **23**, 1696–1718 (2010).
31. I. Harris, T. J. Osborn, P. Jones, D. Lister, Version 4 of the CRU TS monthly high-resolution gridded multivariate climate dataset. *Sci. Data* **7**, 109 (2020).
32. R. Grotjahn, J. Huynh, Contiguous US summer maximum temperature and heat stress trends in CRU and NOAA Climate Division data plus comparisons to reanalyses. *Sci. Rep.* **8**, 11146 (2018).
33. I. R. Simpson, K. A. McKinnon, D. Kennedy, D. M. Lawrence, F. Lehner, R. Seager, Observed humidity trends in dry regions contradict climate models. *Proc. Natl. Acad. Sci. U.S.A.* **121**, e2302480120 (2024).
34. H. Hersbach, B. Bell, P. Berrisford, S. Hirahara, A. Horányi, J. Muñoz-Sabater, J. Nicolas, C. Peubey, R. Radu, D. Schepers, A. Simmons, C. Soci, S. Abdalla, X. Abellan, G. Balsamo, P. Bechtold, G. Biavati, J. Bidlot, M. Bonavita, G. De Chiara, P. Dahlgren, D. Dee, M. Diamantakis, R. Dragani, J. Flemming, R. Forbes, M. Fuentes, A. Geer, L. Haimberger, S. Healy, R. J. Hogan, E. Hólm, M. Janisková, S. Keeley, P. Laloyaux, P. Lopez, C. Lupu, G. Radnoti, P. de Rosnay, I. Rozum, F. Vamborg, S. Villaume, J. N. Thépaut, The ERA5 global reanalysis. *Q. J. Roy. Meteor. Soc.* **146**, 1999–2049 (2020).
35. M. Y. Chen, W. Shi, P. P. Xie, V. B. S. Silva, V. E. Kousky, R. W. Higgins, J. E. Janowiak, Assessing objective techniques for gauge-based analyses of global daily precipitation. *J. Geophys. Res-Atmos* **113**, 10.1029/2007JD009132 (2008).

36. F. T. Wolkeba, M. M. Mekonnen, Evaluation of gridded precipitation data in water availability modeling in CONUS. *J. Hydrol.* **628**, 130575 (2024).
37. S. Z. Dobrowski, J. Abatzoglou, A. K. Swanson, J. A. Greenberg, A. R. Mynsberge, Z. A. Holden, M. K. Schwartz, The climate velocity of the contiguous United States during the 20th century. *Glob. Change Biol.* **19**, 241–251 (2013).
38. G. Bandoc, R. Pravalie, Climatic water balance dynamics over the last five decades in Romania's most arid region, Dobrogea. *J. Geogr. Sci.* **25**, 1307–1327 (2015).
39. M. P. Byrne, P. A. O'Gorman, The response of precipitation minus evapotranspiration to climate warming: Why the "wet-get-wetter, dry-get-drier" scaling does not hold over land. *J. Climate* **28**, 8078–8092 (2015).
40. M. Svoboda, D. LeComte, M. Hayes, R. Heim, K. Gleason, J. Angel, B. Rippey, R. Tinker, M. Palecki, D. Stooksbury, D. Miskus, S. Stephens, The drought monitor. *B. Am. Meteorol. Soc.* **83**, 1181–1190 (2002).
41. R. R. Heim, A review of twentieth-century drought indices used in the United States. *B. Am. Meteorol. Soc.* **83**, 1149–1166 (2002).
42. D. D. Breshears, H. D. Adams, D. Eamus, N. G. McDowell, D. J. Law, R. E. Will, A. P. Williams, C. B. Zou, The critical amplifying role of increasing atmospheric moisture demand on tree mortality and associated regional die-off. *Front. Plant Sci.* **4**, 266 (2013).
43. F. Lehner, C. Deser, I. R. Simpson, L. Terray, Attributing the US Southwest's recent shift into drier conditions. *Geophys. Res. Lett.* **45**, 6251–6261 (2018).
44. D. S. Wilks, On "field significance" and the false discovery rate. *J. Appl. Meteorol. Clim.* **45**, 1181–1189 (2006).
45. J. T. Abatzoglou, A. P. Williams, Impact of anthropogenic climate change on wildfire across western US forests. *Proc. Natl. Acad. Sci. U.S.A.* **113**, 11770–11775 (2016).
46. J. Sheffield, S. J. Camargo, R. Fu, Q. Hu, X. A. Jiang, N. Johnson, K. B. Karnauskas, S. T. Kim, J. Kinter, S. Kumar, B. Langenbrunner, E. Maloney, A. Mariotti, J. E. Meyerson, J. D. Neelin, S. Nigam, Z. T. Pan, A. Ruiz-Barradas, R. Seager, Y. L. Serra, D. Z. Sun, C. Z. Wang, S. P. Xie, J. Y. Yu, T. Zhang, M. Zhao, North American climate in CMIP5 Experiments. Part II: Evaluation of historical simulations of intraseasonal to decadal variability. *J. Climate* **26**, 9247–9290 (2013).
47. S. Gangopadhyay, C. A. Woodhouse, G. J. McCabe, C. C. Routson, D. M. Meko, Tree rings reveal unmatched 2nd century drought in the Colorado River Basin. *Geophys. Res. Lett.* **49**, e2022GL098781 (2022).
48. B. I. Cook, R. L. Miller, R. Seager, Dust and sea surface temperature forcing of the 1930s "Dust Bowl" drought. *Geophys. Res. Lett.* **35**, 10.1029/2008GL033486 (2008).
49. K. Riahi, D. P. van Vuuren, E. Kriegler, J. Edmonds, B. C. O'Neill, S. Fujimori, N. Bauer, K. Calvin, R. Dellink, O. Fricko, W. Lutz, A. Popp, J. C. Cuaresma, K. C. Samir, M. Leimbach, L. W. Jiang, T. Kram, S. Rao, J. Emmerling, K. Ebi, T. Hasegawa, P. Havlik, F. Humpenöder, L. A. da Silva, S. Smith, E. Stehfest, V. Bosetti, J. Eom, D. Gernaat, T. Masui, J. Rogelj, J. Strefler, L. Drouet, V. Krey, G. Luderer, M. Harmsen, K. Takahashi, L. Baumstark, J. C. Doelman, M. Kainuma, Z. Klimont, G. Marangoni, H. Lotze-Campen, M. Obersteiner, A. Tabeau, M. Tavoni, The shared socioeconomic pathways and their energy, land use, and greenhouse gas emissions implications: An overview. *Glob. Environ. Change* **42**, 153–168 (2017).
50. A. J. Cannon, S. R. Sobie, T. Q. Murdock, Bias correction of GCM Precipitation by quantile mapping: How well do methods preserve changes in quantiles and extremes? *J. Climate* **28**, 6938–6959 (2015).
51. M. Wild, Global dimming and brightening: A review. *J. Geophys. Res. Atmos.* **114**, 10.1029/2008JD011470 (2009).
52. D. P. Wang, D. B. Guan, S. P. Zhu, M. M. Kinnon, G. N. Geng, Q. Zhang, H. R. Zheng, T. Y. Lei, S. Shao, P. Gong, S. J. Davis, Economic footprint of California wildfires in 2018. *Nat. Sustain.* **4**, 252–260 (2021).
53. R. J. Qiu, L. G. Li, S. Z. Kang, C. W. Liu, Z. C. Wang, E. P. Cajucom, B. Z. Zhang, E. Agathokleous, An improved method to estimate actual vapor pressure without relative humidity data. *Agric. For. Meteorol.* **298**, 108306 (2021).
54. L. S. Pereira, R. G. Allen, M. Smith, D. Raes, Crop evapotranspiration estimation with FAO56: Past and future. *Agr. Water Manag.* **147**, 4–20 (2015).
55. K. Djaman, M. O'Neill, L. Diop, A. Bodian, S. Allen, K. Koudahe, K. Lombard, Evaluation of the Penman-Monteith and other 34 reference evapotranspiration equations under limited data in a semiarid dry climate. *Theor. Appl. Climatol.* **137**, 729–743 (2019).
56. Q. Yang, Z. G. Ma, Z. Y. Zheng, Y. W. Duan, Sensitivity of potential evapotranspiration estimation to the Thornthwaite and Penman-Monteith methods in the study of global drylands. *Adv. Atmos. Sci.* **34**, 1381–1394 (2017).
57. R. G. Allen, L. S. Pereira, D. Raes, M. Smith, "Crop evapotranspiration-Guidelines for computing crop water requirements - FAO Irrigation and drainage paper 56 (Food and Agriculture Organization, 1998), vol. 300, pp. D05109.
58. R. G. Allen, W. O. Pruitt, J. L. Wright, T. A. Howell, F. Ventura, R. Snyder, D. Itenfisu, P. Steduto, J. Berengena, J. B. Yrisarry, M. Smith, L. S. Pereira, D. Raes, A. Perrier, I. Alves, I. Walter, R. Elliott, A recommendation on standardized surface resistance for hourly calculation of reference ET_0 by the FAO56 Penman-Monteith method. *Agr. Water Manag.* **81**, 1–22 (2006).
59. Q. Chang, D. L. Ficklin, W. Z. Jiao, S. O. Denham, J. D. Wood, N. A. Brunsell, R. Matamala, D. R. Cook, L. X. Wang, K. A. Novick, Earlier ecological drought detection by involving the interaction of phenology and eco-physiological function. *Earths Future* **11**, e2022EF002667 (2023).
60. Z. T. Zhang, K. C. Wang, Quantify uncertainty in historical simulation and future projection of surface wind speed over global land and ocean. *Environ. Res. Lett.* **19**, 054029 (2024).
61. A. Berg, K. A. McColl, No projected global drylands expansion under greenhouse warming. *Nat. Clim. Change* **11**, 331–337 (2021).
62. R. Seager, N. Henderson, M. A. Cane, H. B. Liu, J. Nakamura, Is there a role for human-induced climate change in the precipitation decline that drove the california drought? *J. Climate* **30**, 10237–10258 (2017).
63. D. L. Swain, D. E. Horton, D. Singh, N. S. Diffenbaugh, Trends in atmospheric patterns conducive to seasonal precipitation and temperature extremes in California. *Sci. Adv.* **2**, e1501344 (2016).
64. D. E. Horton, N. C. Johnson, D. Singh, D. L. Swain, B. Rajaratnam, N. S. Diffenbaugh, Contribution of changes in atmospheric circulation patterns to extreme temperature trends. *Nature* **522**, 465–469 (2015).
65. D. Faranda, G. Messori, A. Jezequel, M. Vrac, P. Yiou, Atmospheric circulation compounds anthropogenic warming and impacts of climate extremes in Europe. *Proc. Natl. Acad. Sci. U.S.A.* **120**, e2214525120 (2023).
66. S. Zhou, A. P. Williams, A. M. Berg, B. I. Cook, Y. Zhang, S. Hagemann, R. Lorenz, S. I. Seneviratne, P. Gentine, Land-atmosphere feedbacks exacerbate concurrent soil drought and atmospheric aridity. *Proc. Natl. Acad. Sci. U.S.A.* **116**, 18848–18853 (2019).
67. C. R. Schwalm, S. Glendon, P. B. Duffy, RCP8.5 tracks cumulative CO_2 emissions. *Proc. Natl. Acad. Sci. U.S.A.* **117**, 19656–19657 (2020).
68. N. Christidis, P. A. Stott, Changes in the geopotential height at 500hPa under the influence of external climatic forcings. *Geophys. Res. Lett.* **42**, 10798–10806 (2015).
69. N. Siler, C. Proistosescu, S. Po-Chedley, Natural variability has slowed the decline in western US snowpack since the 1980s. *Geophys. Res. Lett.* **46**, 346–355 (2019).
70. D. L. Ficklin, J. T. Abatzoglou, S. M. Robeson, A. Dufficy, The influence of climate model biases on projections of aridity and drought. *J. Climate* **29**, 1269–1285 (2016).
71. A. C. F. Xavier, L. L. Martins, A. P. Rudke, M. V. B. de Morais, J. A. Martins, G. C. Blain, Evaluation of Quantile Delta Mapping as a bias-correction method in maximum rainfall dataset from downscaled models in São Paulo state (Brazil). *Int. J. Climatol.* **42**, 175–190 (2022).
72. C. W. Thornthwaite, An approach toward a rational classification of climate. *Geogr. Rev.* **38**, 55–94 (1948).
73. J. Sheffield, E. F. Wood, M. L. Roderick, Little change in global drought over the past 60 years. *Nature* **491**, 435–438 (2012).
74. T. Iizumi, H. Takikawa, Y. Hirabayashi, N. Hanasaki, M. Nishimori, Contributions of different bias-correction methods and reference meteorological forcing data sets to uncertainty in projected temperature and precipitation extremes. *J. Geophys. Res. Atmos.* **122**, 7800–7819 (2017).
75. Y. Z. Zhuang, R. Fu, H. Q. Wang, Large-scale atmospheric circulation patterns associated with US Great Plains warm season droughts revealed by self-organizing maps. *J. Geophys. Res. Atmos.* **125**, e2019JD031460 (2020).
76. A. Jézéquel, P. Yiou, S. Radanovics, Role of circulation in European heatwaves using flow analogues. *Clim. Dynam.* **50**, 1145–1159 (2018).
77. C. Deser, L. Terray, A. S. Phillips, Forced and internal components of winter air temperature trends over North America during the past 50 Years: Mechanisms and implications. *J. Climate* **29**, 2237–2258 (2016).
78. Y. Z. Zhuang, R. Fu, Quantifying the contribution of atmospheric circulation to precipitation variability and changes in the US Great Plains and southwest using self-organizing map-analogue. *Atmos. Chem. Phys.* **24**, 1641–1657 (2024).
79. S. Sippel, N. Meinshausen, E. M. Fischer, E. Székely, R. Knutti, Climate change now detectable from any single day of weather at global scale. *Nat. Clim. Change* **10**, 35–41 (2020).
80. R. E. Livezey, W. Y. Chen, Statistical field significance and its determination by Monte-Carlo techniques. *Mon. Wea. Rev.* **111**, 46–59 (1983).
81. NOAA National Centers of Environmental Information, Global Surface Summary of the Day - GSOD. 1.0 (NOAA National Centers for Environmental Information, 1999).
82. J. Muñoz-Sabater, E. Dutra, A. Agustí-Panareda, C. Albergel, G. Arduini, G. Balsamo, S. Boussetta, M. Choulga, S. Harrigan, H. Hersbach, B. Martens, D. G. Miralles, M. Piles, N. J. Rodríguez-Fernández, E. Zsoter, C. Buontempo, J. N. Thépaut, ERA5-land: A state-of-the-art global reanalysis dataset for land applications. *Earth Syst. Sci. Data* **13**, 4349–4383 (2021).
83. M. Rodell, P. R. Houser, U. Jambor, J. Gottschalck, K. Mitchell, C. J. Meng, K. Arsenault, B. Cosgrove, J. Radakovich, M. Bosilovich, J. K. Entin, J. P. Walker, D. Lohmann, D. Toll, The global land data assimilation system. *B. Am. Meteorol. Soc.* **85**, 381–394 (2004).
84. B. Martens, D. G. Miralles, H. Lievens, R. van der Schalie, R. A. M. de Jeu, D. Fernández-Prieto, H. E. Beck, W. A. Dorigo, N. E. C. Verhoest, GLEAM v3: Satellite-based land evaporation and root-zone soil moisture. *Geosci. Model Dev.* **10**, 1903–1925 (2017).

85. D. G. Miralles, T. R. H. Holmes, R. A. M. De Jeu, J. H. Gash, A. G. C. A. Meesters, A. J. Dolman, Global land-surface evaporation estimated from satellite-based observations. *Hydrol. Earth Syst. Sci.* **15**, 453–469 (2011).
86. K. A. Dunne, C. J. Willmott, Global distribution of plant-extractable water capacity of soil. *Int. J. Climatol.* **16**, 841–859 (1996).
87. A. G. Dai, Characteristics and trends in various forms of the Palmer Drought Severity Index during 1900-2008. *J. Geophys. Res. Atmos.* **116**, 10.1029/2010JD015541 (2011).
88. A. P. Williams, C. D. Allen, A. K. Macalady, D. Griffin, C. A. Woodhouse, D. M. Meko, T. W. Swetnam, S. A. Rauscher, R. Seager, H. D. Grissino-Mayer, J. S. Dean, E. R. Cook, C. Gangodagamage, M. Cai, N. G. McDowell, Temperature as a potent driver of regional forest drought stress and tree mortality. *Nat. Clim. Change* **3**, 292–297 (2013).
89. C. D. Allen, D. D. Breshears, N. G. McDowell, On underestimation of global vulnerability to tree mortality and forest die-off from hotter drought in the Anthropocene. *Ecosphere* **6**, 1–55 (2015).
90. H. Hartmann, H. D. Adams, W. R. L. Anderegg, S. Jansen, M. J. B. Zeppel, Research frontiers in drought-induced tree mortality: Crossing scales and disciplines. *New Phytol.* **205**, 965–969 (2015).
91. G. W. Moore, C. B. Edgar, J. G. Vogel, R. A. Washington-Allen, O. G. March, R. Zehnder, Tree mortality from an exceptional drought spanning mesic to semiarid ecoregions. *Ecol. Appl.* **26**, 602–611 (2016).
92. N. McDowell, C. D. Allen, K. Anderson-Teixeira, P. Brando, R. Brienen, J. Chambers, B. Christoffersen, S. Davies, C. Doughty, A. Duque, F. Espirito-Santo, R. Fisher, C. G. Fontes, D. Galbraith, D. Goodsman, C. Grossiord, H. Hartmann, J. Holm, D. J. Johnson, A. Kassim, M. Keller, C. Koven, L. Kueppers, T. Kumagai, Y. Malhi, S. M. McMahon, M. Mencuccini, P. Meir, P. Moorcroft, H. C. Muller-Landau, O. L. Phillips, T. Powell, C. A. Sierra, J. Sperry, J. Warren, C. G. Xu, X. T. Xu, Drivers and mechanisms of tree mortality in moist tropical forests. *New Phytol.* **219**, 851–869 (2018).
93. C. G. Fontes, T. E. Dawson, K. Jardine, N. McDowell, B. O. Gimenez, L. Anderegg, R. Negron-Juarez, N. Higuchi, P. V. A. Fine, A. C. Araújo, J. Q. Chambers, Dry and hot: The hydraulic consequences of a climate change-type drought for Amazonian trees. *Philos. T. R. Soc. B* **373**, 20180209 (2018).
94. C. Grossiord, T. N. Buckley, L. A. Cernusak, K. A. Novick, B. Poulter, R. T. W. Siegwolf, J. S. Sperry, N. G. McDowell, Plant responses to rising vapor pressure deficit. *New Phytol.* **226**, 1550–1566 (2020).

Acknowledgments: We thank the reviewers for insightful comments and R. E. Dickinson for his constructive feedback, both of which have substantially improved this manuscript. The statements, findings, conclusions, and recommendations are those of the authors and do not necessarily reflect the views of NOAA or the US Department of Commerce. **Funding:** This work was supported by the National Oceanic and Atmospheric Administration, grant NA20OAR4310426 (R.F. and Y.Z.); National Science Foundation, grant AGS-2214697 (R.F. and Y.Z.); and National Oceanic and Atmospheric Administration, cooperative agreement NA22OAR4320151 (J.L. and A.M.S.). **Author contributions:** Conceptualization: R.F., Y.Z., J.L., A.M.S., B.A.P., and G.D. Data curation: Y.Z. and R.F. Formal analysis: Y.Z. Funding acquisition: R.F. and A.M.S. Investigation: Y.Z. and R.F. Methodology: Y.Z., R.F., and A.M.S. Project administration: R.F. Resources: R.F. and Y.Z. Software: Y.Z. Supervision: R.F. Validation: Y.Z. Visualization: Y.Z., R.F., and J.L. Writing—original draft: Y.Z. and R.F. Writing—review and editing: Y.Z., R.F., J.L., A.M.S., B.A.P., and G.D. **Competing interests:** The authors declare that they have no competing interests. **Data and materials availability:** All data needed to evaluate the conclusions in the paper are present in the paper and/or the Supplementary Materials. The data that support the findings of this study are publicly available. The CPC precipitation data are obtained from the NOAA Physical Sciences Laboratory (PSL)'s website at https://psl.noaa.gov/data/gridded/data.unified.daily.conus.html. The ERA5 data are retrieved from the Copernicus Climate Change Service (C3S) Climate Data Store (CDS) at https://cds.climate.copernicus.eu. The CMIP6 data are taken from the Earth System Grid Federation (ESGF) MetaGrid at https://aims2.llnl.gov/search/cmip6. The GSOD data are obtained from NOAA National Centers for Environmental Information (NCEI)'s website at www.ncei.noaa.gov/data/global-summary-of-the-day/archive/. The CRU TS v4.07 data are obtained from https://crudata.uea.ac.uk/cru/data/hrg/. Soil moisture data are from three sources, including ERA5-Land (https://cds.climate.copernicus.eu/), GLDAS Noah Land Surface Model v2.0 and v2.1 (https://disc.gsfc.nasa.gov/), and GLEAM v3.8a (www.gleam.eu/). The code and data that we used to perform QDM are deposited at https://zenodo.org/doi/10.5281/zenodo.13836244. All other methodologies/codes central to this study are described in the paper and/or Supplementary Materials with references.

Submitted 8 January 2024
Accepted 2 October 2024
Published 6 November 2024
10.1126/sciadv.adn9389